Boundary Condition Modifications of the Suzen-Huang Plasma Actuator Model

Imran H. Ibrahim[1] and Martin Skote*,[1]
[1]School of Mechanical & Aerospace Engineering, Nanyang Technological University,
50 Nanyang Avenue, Singapore 639798.
Tel: +6567904271/ Fax: +6567924062

ABSTRACT

The accuracy of the Suzen-Huang (S-H) model is improved by altering the boundary condition of the dielectric surface above the lower electrode. For the equation governing the electric field, we introduce a 'dielectric shielding' condition at the same region, which results in a spread of the electric field strength along the dielectric surface. For the equation governing the surface charge density, we introduce boundary conditions that modify the behavior of the charge density variable in the S-H model. The conditions represent a fitting procedure by adding the features of propagation and dissipation in a one-dimensional Fokker-Plank equation. The equation is initiated by a normal distribution function centered at the leading edge of the lower electrode. These modifications improved model results by about 50% when comparing the maximum induced velocity value with experimental results. Furthermore, charge density growth is propagating in a similar manner to that obtained by charge transport models.

Key Words: plasma actuator, computational modelling, Debye length, charge density

1. INTRODUCTION

The plasma actuator is a modern form of flow control device, and advantages include the capability of affecting flow in real-time and having no moving parts [1, 2]. The multitude of parameters involved in the design of the plasma actuator points to the use of CFD as a tool in the design process. Experimental methods pose a disadvantage because they result in high costs when designing actual geometries and data.

The computational models have evolved from the late 1990s till today. Generally, all computational models require a coupling of the 'plasma' equations with the 'flow' equations. The Lorentz force that is produced by the 'plasma' equations are inserted to the body force term in the Navier-Stokes equations. Two forms of plasma actuator modelling can be derived from the existing modelling techniques: the microscopic or charge transport [3–5] and macroscopic or physics-based form [6–8]. These terms microscopic/charge transport and macroscopic/ physics-based will be used interchangeably in the paper. The microscopic model captures the motion of the charge particles by coupling the drift-diffusion equation with the Maxwell equation. The time scale defining a microscopic plasma process is about 10^{-8} to 10^{-9} s, which is in the same order of the mobility of charged particles. The macroscopic form captures the essential physics of the flow by modelling the electric potential characteristics derived from the Maxwell equations. The time scale involved in this process is normally about 10^{-4} s, which is defined by the frequency of the AC voltage required to power the actuator. The characteristic length scale for both the microscopic and macroscopic forms are obtained from the Debye lengths of the simulation, which is about 10^{-4} m.

One of the earlier charge transport modelling was conducted by Massines et al. [3]. It consisted of a one-dimensional model based on simultaneous solution of continuity equations for charged particles and the Maxwell equation. The study conducted by Boeuf et al. [4] considered nitrogen and oxygen at atmospheric pressure. The model included other complicated gas chemistry which has 230 reaction equations. A study by Rouffet [5] consisted of a mixture of ions, electrons and neutral molecules. The model was made up of the drift-diffusion and the Maxwell equation (Gauss's law) for the electrons and ions as shown below:

$$\frac{\partial n_e}{\partial t} + \nabla \cdot \left[-n_e \mu_e \boldsymbol{E} - D_e \nabla n_e \right] = n_e v_i - r m_e n_i \tag{1}$$

Corresponding author. E-mail: mskote@ntu.edu.sg

$$\frac{\partial n_i}{\partial x} + \nabla \cdot \left[n_i \mu_i \boldsymbol{E} - D_i \nabla n_i \right] = n_e v_i - m_e n_i \tag{2}$$

$$\nabla \cdot (\varepsilon \boldsymbol{E}) = \frac{e}{\varepsilon_0} \left(n_i - n_e \right) \tag{3}$$

$$\boldsymbol{F}_b = \rho_c \boldsymbol{E} = e \left(n_i - n_e \right) \nabla \Phi \tag{4}$$

The influence on airflow due to the body force is accounted for by including the body force in the Navier-Stokes equations:

$$\rho \frac{\partial U}{\partial t} + \nabla \left(\eta \nabla U \right) + \rho (U \cdot \nabla) U + \nabla \mathrm{p} = e \left(n_i - n_e \right) \nabla \Phi \tag{5}$$

$$\nabla \cdot U = 0 \tag{6}$$

Another approach to modelling the body force of the plasma actuator was through time-averaging, as done by Roy et al. [9]. The first-principle based electrohydrodynamic force modelling technique used in their study was basically an average solution obtained from a charge transport modelling technique by Singh et al. [10].

The first physics-based model was done by Roth et al. [6] who introduced the paraelectric and peristaltic (OAUGDP^{TM}) forms of DBD actuator. Their team used a simple method to calculate body force which was proportional to the squared electric field and the vacuum permittivity. Eqn (7) shows this relation:

$$\boldsymbol{F}_b = \frac{1}{2} \left(\varepsilon_0 \boldsymbol{E}^2 \right) \tag{7}$$

Further analysis by Enloe et al. [11] showed that there is an inaccuracy in the body force estimation made by Roth. The assumption made for the gradient of the electric field was for one-dimensional flow and rested on the assertion that

$$\nabla \boldsymbol{E}^2 = 2 \boldsymbol{E} \left(\nabla \cdot \boldsymbol{E} \right) \tag{8}$$

which was true only for a one-dimensional flow and did not apply for the aerodynamic plasma actuator. Shyy et al. [12] presented a model which was based on the assumption that the electric-field strength $|\boldsymbol{E}|$ decreased linearly from the edge of the upper electrode to the extent of the lower electrode. The variation of $|\boldsymbol{E}|$ can be written as:

$$|E| = E_0 - k_1 x - k_2 y \tag{9}$$

where constants k_1 and k_2 are determined by using breakdown electric field strength values at the plasma-fluid boundary. The final body force form is written as:

$$\boldsymbol{F}_{tave} = \vartheta \alpha \rho_c e_c \Delta t \boldsymbol{E} \delta \tag{10}$$

A review by Corke et al. [2] mentioned that the linear electric field assumption was not consistent with results of experiments conducted by their group [13–15]. The results showed that there was an

exponential decay in electric-field strength. The same review mentioned a later model by Orlov et al. [7] which did not use this assumption and was derived based on the relations of the species charged densities with the Boltzmann equation and temperature with the Debye length variables was introduced. The model is based on the fact that the net charge density at any point in the plasma is proportional to the potential at that point and is written as:

$$\boldsymbol{F}_b = \rho_c \boldsymbol{E} = -\left(\frac{\varepsilon_0}{\lambda_D^2}\right)\Phi \boldsymbol{E} \tag{11}$$

Finally, the plasma actuator model designed by Suzen and Huang [8] (hereafter abbreviated as S-H) studied the implication of splitting the total electric potential term Φ into two parts: one being influenced by external electric field ϕ, and the other potential affected by the net charge density φ. This technique had been applied to turbine blades [8, 16–18] to achieve reduction in flow separation. The equations are shown as:

$$\Phi = \phi + \varphi \tag{12}$$

$$\nabla \cdot (\varepsilon_r \nabla \phi) = 0 \tag{13}$$

$$\nabla \cdot (\varepsilon_r \nabla \varphi) = \rho_c / \varepsilon_0 \tag{14}$$

$$\rho_c / \varepsilon_0 = \left(-1 / \lambda_D^2\right)\varphi \tag{15}$$

In short, the equations are solved to obtain the Lorentz body force:

$$\boldsymbol{F}_b = \rho_c(-\nabla \phi) \tag{16}$$

and the details will be discussed in section 4.

We have used this modelling technique in our simulations because of two reasons. Firstly, a physics-based model requires less computing costs compared to a charge transport model. This allows the simulations to be a part of the design stage for an iterative optimization concept of plasma actuator applications as mentioned in Corke et al. [2]. Secondly, the S-H modelling technique allows the representation of the charge density on the top of the encapsulated electrode to be controlled. This ability is an appealing feature in the S-H model compared to other models because it shows good potential in providing an idealized model which encompasses both microscopic and macroscopic plasma actuator modelling characteristics.

The two reasons above are the foundation for the purpose of our work; which is to model the effects of the plasma on the flow in the context of the fluid dynamics. We provide improvements to the boundary conditions of the S-H model by introducing a ‘dielectric shielding’ condition for the equation governing the electric field, and a Fokker-Planck augmentation to the equation governing the surface charge density. These two modifications result in better agreements between model results and experimental data.

In the first two studies by Suzen et al. [8, 16], a half normal distribution was prescribed along the lower electrode as a weighting function for the surface charge. The surface charge only propagated in the normal direction relative to the dielectric. This prescription was absent in a later study by Suzen et al. [17] because it was assumed that the embedded electrode was the source for the charge density and that the solution will automatically result in a charge density distribution similar to that of a half normal distribution. The alternate boundary condition that we propose invokes the use of the half normal distribution with drift-diffusive characteristics derived from the Fokker-Planck equation. This fitting procedure is not dissimilar to that used by Corke’s group in the definition of the boundary condition at the dielectric surface. In the model proposed by Corke, an electric circuit model of the surface charge propagation was used along the dielectric surface. Time-varying electric potential characteristics were then obtained. Similar studies have also been done by Shyy et al. [12] and Grundmann et al. [19].

The time-varying characteristics of the surface charge densities that we propose have not been studied before in the S-H models. The effects on body force and induced velocities are analysed with the addition of this new condition. The improved results are demonstrated for a model problem of a fundamental character — the Single Dielectric Barrier Discharge (SDBD). It is our hope that with the new boundary condition, plasma actuator modelling predictions within flow control community will be more reliable and useful than previously possible.

We have provided a brief introduction of plasma actuator modelling in the introduction. In the next section, we will discuss the simulation setup of the original and modified S-H model. Following that, we will describe the computational resources used in our simulations before analyzing the results gathered. In the final section, we will conclude by providing a summary and recommendations for future work.

3. SIMULATION SETUP

The simulations conducted were based on the geometries specified in Suzen et al. [17]. The domain, shown in Figure 1, consists of two subdomains, air and a dielectric, Kapton. The air subdomain was rectangular with a 0.06 m (length) by 0.1 m (width). The Kapton is similarly rectangular shaped with a width of 1×10^{-3} m. The electrodes are 0.01 m by 10^{-4} m. The upper electrode is placed at the 0.01 m tick, while the lower electrode was placed 10^{-4} m under the dielectric at the 0.0205 m tick. A gap size of 5×10^{-4} m existed between the upper and lower electrode. Figure 2 shows a zoomed image of the gap between the two electrodes.

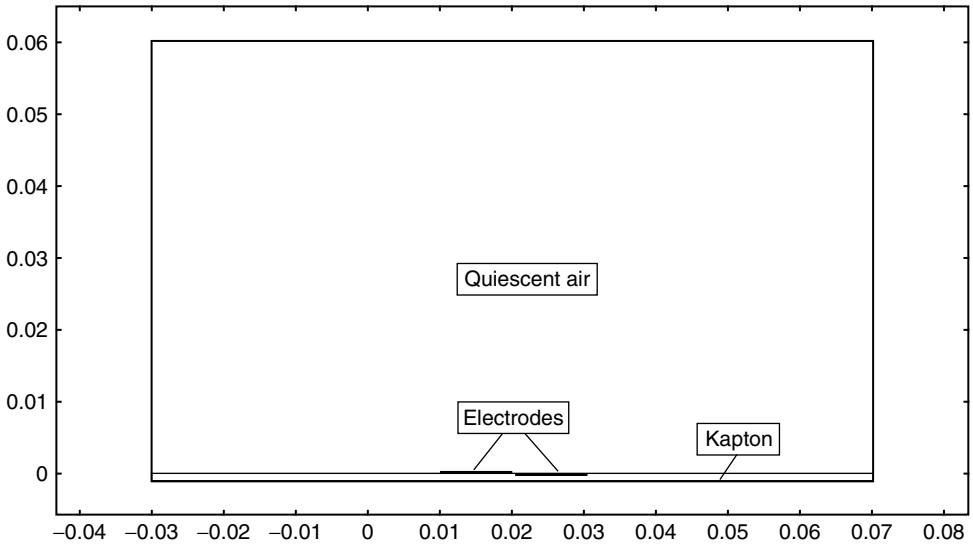

Figure 1. Simulation domain used by Suzen et al. [8].

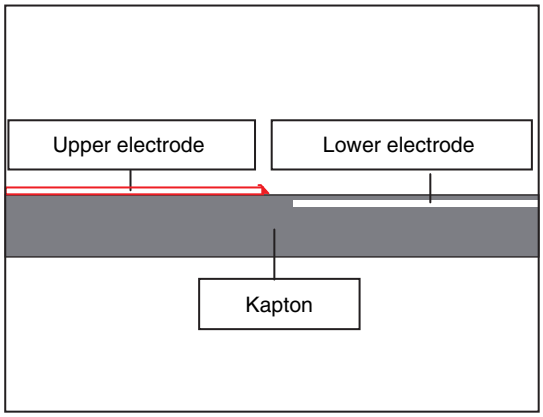

Figure 2. A zoomed-in image of the two electrodes in the simulated domain.

4. NON-DIMENSIONALISED FORM

Details of the derivation of the S-H model can be found in Suzen et al. [8]. We proceed in the details of the non-dimensionalised form of the S-H model. This section is crucial for the application of time-varying surface charge boundary condition which will be mentioned later in section 5.

Eqns (13) and (14) can be solved initially before the Navier-Stokes equation as these equations do not contain a time derivative term. This is done by writing the terms into a non- dimensionalised form. The variables ϕ and ρ_c are non-dimensionalised to their values at the upper and lower electrodes respectively. The term ϕ_o is set as a boundary condition and refers to the applied AC voltage at upper electrode:

$$\phi_0(\tau) = \phi_{\max} \times f(\tau) \tag{17}$$

where $\phi_{\max}$ (V) refers to the maximum amplitude of the AC voltage supplied.

The term $\rho_{c,\,o}$ is set as a boundary condition at the lower electrode as:

$$\rho_c(\tau) = \rho_{c,\max} \times f(\tau) \tag{18}$$

where $\rho_{c,\max}$ (C/m^3) refers to the maximum charge density of the AC voltage supplied.

The function $f(\tau)$ for the AC voltage source is:

$$f(\tau) = \sin(2\pi\tau) \tag{19}$$

where τ refers to a nondimensionalised time quantity.

We introduce the quantity by relating it to the frequency ω as:

$$\tau = \omega t \tag{20}$$

where ω (Hz) refers to the frequency of the AC voltage supply and is equal to 4.5 kHz in experiments [20, 21]. We also relate the frequency to the characteristic time, t_c as:

$$\omega = \frac{1}{t_c} \tag{21}$$

where $t_c = 2.22 \times 10^{-4}$ s. Note that this characteristic time is the time taken to complete one sinusoidal cycle and has the same order of 10^{-4} s as used in Enloe et al. [11]. The simulations are run in the nondimensionalised time quantity, τ, from a value of 0 to 1. A time step of 0.1 is chosen to adequately observe the evolution of the four variables of interests: electric field, charge density, body force and induced velocity.

The resulting non-dimensionalised quantities are:

$$\phi^* = \phi / \phi_0(\tau) \tag{22}$$

$$\rho_c^* = \rho_c / \rho_{c,0}(\tau) \tag{23}$$

$$F_b^* = F_b / \left(\rho_{c,\max} \times \phi_{\max}\right) \tag{24}$$

Therefore eqn (13) becomes:

$$\nabla \cdot \left(\varepsilon_r \nabla \phi^* \right) = 0 \tag{25}$$

And eqn (14):

$$\nabla \cdot \left(\varepsilon_r \nabla \rho_c^* \right) = \rho_c^* / \lambda_D^2 \tag{26}$$

The boundary condition for the upper electrode for ϕ^* is set to unity so that once ϕ^* is determined, the dimensional value ϕ can be obtained at any given time by multiplying the distribution with the corresponding value $\phi(\tau)$ given by eqn (17). Similarly, the boundary condition for the lower electrode for ρ_c^* is set to unity. This allows the dimensional value ρ_c to be obtained by multiplying the non-dimensionalised distribution ρ_c^* with the corresponding value $\rho_{c,o}(t)$ given in eqn (23).

The characteristic λ_D used for industrial plasma engineering in Roth [22] is approximately 1.7×10^{-4} m and the maximum charged density, $\rho_{c,max}$, as used in a previous simulation by Suzen et al. [17] was set to 0.0075 C/m^3. Previous studies have also shown that the two values could be altered to match the velocity profiles of experimental data.

The maximum amplitude of the AC voltage supplied, ϕ_{max}, is set as 5 kV. Eqns (25) and (26) are the governing equations used to model the non-dimensionalised body force in COMSOL and are solved separately from the Navier Stokes equations. The dimensionalised body force can be obtained from eqn (24) and is inserted into the Navier-Stokes computations as eqn (16).

Finally, the governing eqns (25), (26) and their boundary equations are shown together with the geometries in Figure 3 and Figure 4 respectively. The terms GE and BC refer to governing equation and boundary conditions respectively. Next we introduce the modification to the boundary condition.

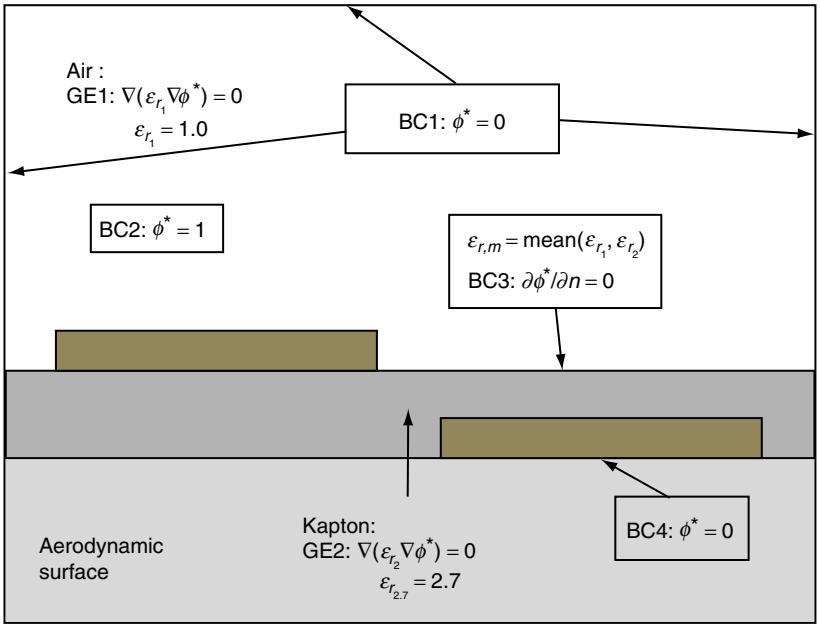

Figure 3. Governing eqns (25) for the S-H model. The illustration is not drawn in scale with simulation.

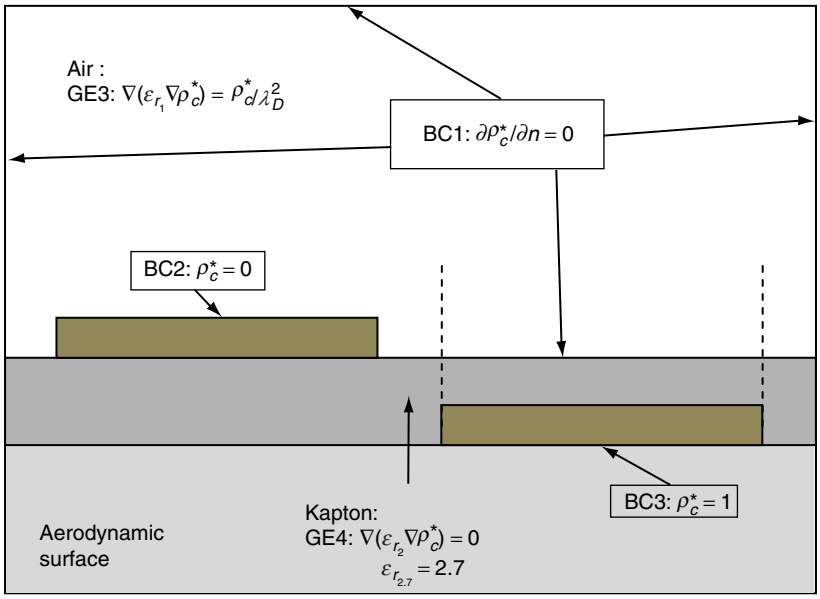

Figure 4. Governing eqns (26) for the S-H model. The illustration is not drawn in scale with simulation.

5. BOUNDARY CONDITION MODIFICATIONS

The 'dielectric shielding' condition for the non-dimensionalised electric potential shown as BC3 in Figure 5 describes a thin layer of thickness λ_D and relative bulk permittivity $\varepsilon_{r,m}$. The term ∇_t describes the tangential derivative of the non-dimensionalised electric potential variable. The condition equates the normal distribution of the surface charge density to the tangential electric field distribution.

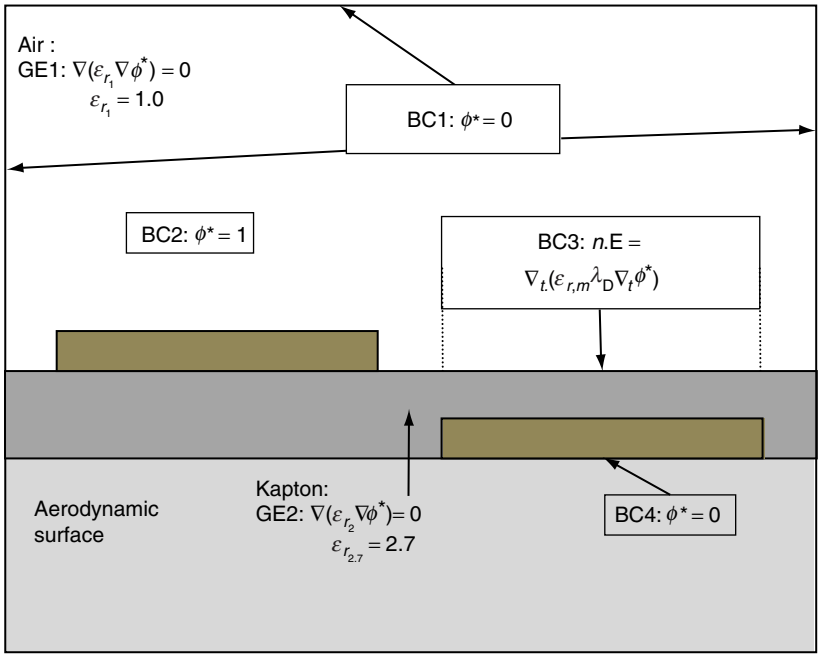

Figure 5. Governing equations for the ϕ^* equation in S-H model. The modified boundary condition is placed at the lower boundary as shown.

For the equation governing the non-dimensionalised charge density, the original boundary condition (BC3 in Figure 4) used in the S-H model resulted in an instantaneous charge density growth along the boundary of the lower electrode that propagates in the normal direction (upwards) of the dielectric surface. This propagation direction is different to the results obtained by charge transport models, where propagation towards the right-side of the exposed electrode was obtained. This motion of the surface charge corresponds to the physics of the plasma actuator, in which streamers originate from the exposed electrode and travels along the dielectric surface [4]. These streamers dissipate and propagate from the exposed electrode and have not been shown in previous S-H models.

The dissipation and propagation characteristics can be modelled by the solution to the one-dimensional Fokker-Planck equation, which is written as:

$$\frac{\partial f}{\partial t} = -D_1 \frac{\partial f}{\partial x} + D_2 \frac{\partial^2 f}{\partial x^2} \tag{27}$$

where D_1 and D_2 corresponds to drift and diffusion constants.

Figure 7 shows a one-dimensional representation of a normal distribution function exhibiting characteristics of eqn (27). The value of the constants D_1 and D_2 are assigned set to unity. The Dirichlet boundary conditions are inserted at both ends of the one-dimensional analysis. The figure shows that the function is initially (at t_1) at a maximum, dissipating and propagating in time. The dissipation is manfested by the decreasing peaks of each successive time step. Similarly, propagation can be observed by the increasing x-coordinates of the dashed lines, which indicate the horizontal locations of the peaks.

To replicate these characteristics in our new boundary condition, two boundary conditions are inserted to reproduce the characteristics shown in Figure 7 and are named BC1 and BC2. They form a new boundary condition (BC) which is obtained by multiplying BC1 and BC2 as shown in Figure 6. These boundary conditions are written as:

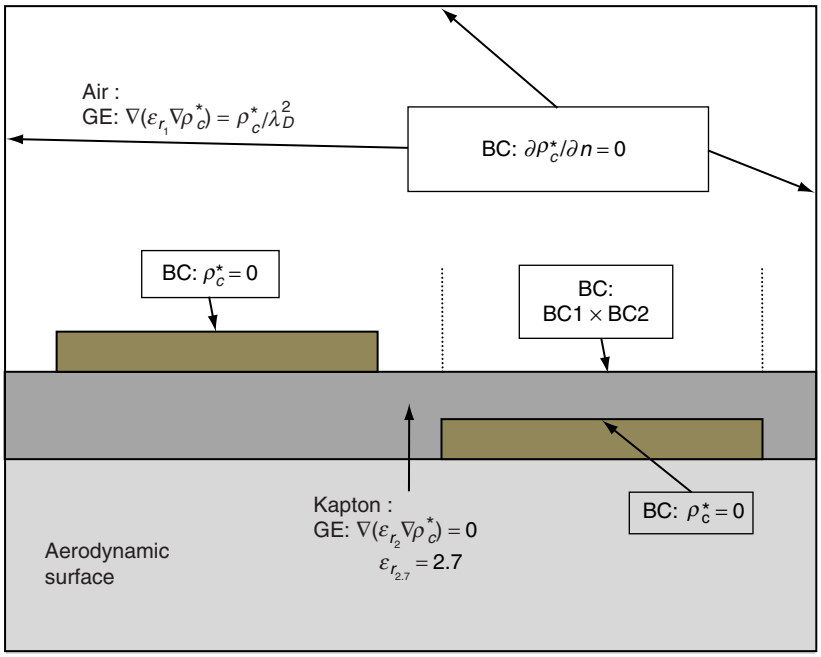

Figure 6. Governing equations for the ρ_c^* equation in S-H model. The modified boundary condition is placed at the lower boundary as shown.

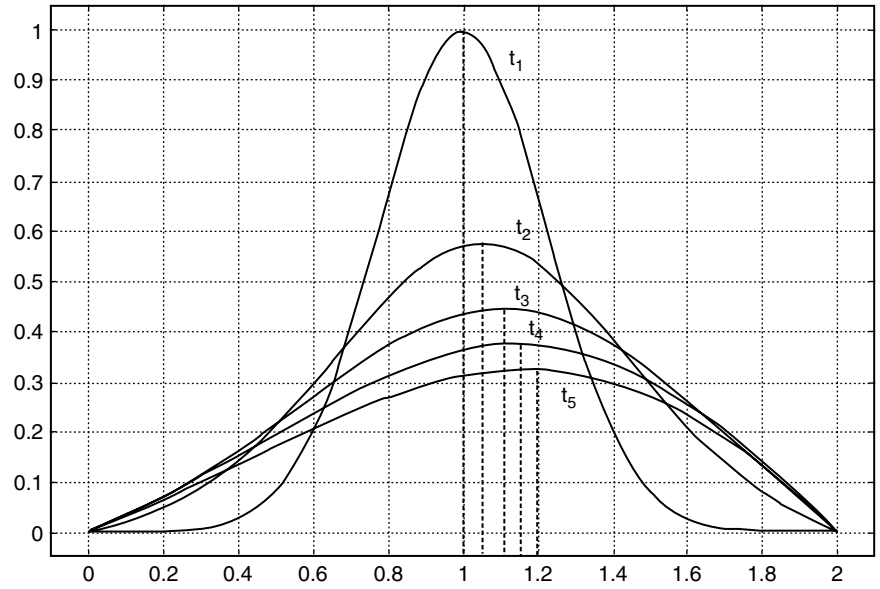

Figure 7. A graphical representation of the one-dimensional Fokker-Planck equation, with increasing time (t_1) to (t_5).

BC1:

$$\exp\left(-\frac{\left(\frac{x-x_1}{x_2}\right)^2}{2\sigma^2}\right) \tag{28}$$

BC2:

$$\begin{matrix}\exp\left(-\left(x-x_1\right)-\tau\right) & x > x_1 \\ 0 & x \le x_1\end{matrix} \tag{29}$$

where x_1 is the x-coordinate of the left (leading) edge of the encapsulated electrode. In our simulation, the value x_1 is 0.0205 m. The terms x_2 and σ are determined by the width of the normal distribution function and are taken as 2×10^{-3} m and 0.3 respectively.

The condition BC1 is the normal distribution function in its initial form (shown as t_1 in Figure 7). The maximum is centered at the x_1 and will be shown in Figure 12. The condition BC2 is a time-varying function which results in a propagation of the surface charge density to the extent of the lower electrode. To produce only a half normal distribution, the condition has to be further reduced into two cases, before and after x_1. The product of BC1 and BC2 will result in the time-varying characteristics with a limit to only occur after the coordinate x_1.

The results in section 7 will validate our boundary condition implementations. In the next section, the computational resources used in our simulations are presented.

6. COMPUTER RESOURCES

Since the problem was electrostatic and fluid dynamic in nature, we have used a software capable of handling the multiphysics features, COMSOL 4.2 [23]. The system used for the COMSOL simulations was a Dell workstation model E5520 with dual quad-core processors running at 2.26 GHz. The

workstation had 24 GB of installed memory (RAM) and used Windows 7 Professional as its operating system.

The simulations were solved using the finite element computational package, COMSOL Multiphysics™ 4.2. The ruling application mode for the investigation was the Incompressible Navier-Stokes application. The solver settings were based on the ruling application model. The application mode also used Lagrange p2-p1 elements to stabilize the pressure. Thus 2nd-order Lagrange elements modelled the velocity components while linear elements modelled the pressure.

The step converges if the following condition was met:

$$\left(\frac{1}{N} \sum \left(\frac{|E_i|}{A_i + R|U_i|} \right)^2 \right)^{1/2} < 1 \tag{30}$$

where A_i is the absolute tolerance for degree of freedom *i*, *R* is the relative tolerance and *N* is the number of degrees of freedom. The estimated local error is typically of the same order of magnitude as the true global error [23]. The method used to solve the time-dependent problem was the backward differentiation formula (BDF) which is a robust method that is commonly used for a wide range of problems. The algorithm for this method can be further studied in Hindmarsh et al. [24].

The Navier-Stokes equation in COMSOL used three artificial diffusion techniques: the Galerkin Least-Squares (GLS), crosswind and isotropic diffusion [23]. These techniques added terms to the transport equation to stabilize the solution. The GLS technique is a form of streamline diffusion that adds higher-ordered superviscosity terms and provides extra stability. Crosswind diffusion addresses the sharp gradients that may occur during the simulation. The terms add diffusion orthogonal to the streamline direction and are mostly consistent and do not alter the equation. The isotropic diffusion technique introduces an artificial diffusion coefficient to the Peclet number so that it never exceeds unity.

A mesh refinement analysis defined in steps by Celik [25] was conducted on the unstructured mesh simulations. The 'maximum element size' parameter in COMSOL is specified in a linear decreasing manner for a structured refinement analysis. A wide range of grid analysis was conducted with emphasis on refinement near the electrodes, as shown in Figure 8. The values of electric potential and charge densities are expected to be at high transients within the vicinity of the electrodes. The high transience would also result in the largest induced velocity gradients. Table 1 shows the six mesh settings used in the analysis and the corresponding Degrees of Freedoms (DoFs). In each setting, a decreasing maximum boundary element size is shown. Figure 9 shows the monotonic convergence of the induced velocity. The induced velocity reaches a plateau at case study d, corresponding to 72694 meshes. The induced velocity plateaus at a magnitude of about 1.36 m/s.

The results of the GCI study are tabulated in Table 2. The largest error occurs from study 3 and 4, with numerical uncertainty of the fine-grid (N_5) solution is reported as 2.66%. This shows that the error estimation is within normal engineering practices of +/– 5%. Although it can be seen from Figure 9 and Table 2 that using a grid size of 72694 is sufficient to produce an accurate solution, the choice of the finest grid size of 247503 is used, so that the criteria of minimum Debye length of about 10^{-4} m near the vicinity of the electrodes is satisfied. Similar conclusions were drawn in the grid independence study by Imran and Skote [26].

An analysis of the velocity profile at the last station (1.6 cm downstream of the electrodes interface) is also conducted. A cut line of the station can be denoted as the jagged line in Figure 10, indicating that the last station is at x = 0.036 m. The horizontal velocity profiles for two different mesh settings and the experimental results are shown in Figure 11. The results indicate that the mesh setting of 247503 elements results in a velocity profile that closely resembles that obtained by experimental results. The curvature at the maximum velocity was about 1 m/s. At the mesh setting for 72694 elements, a maximum value of 0.7 m/s was obtained.

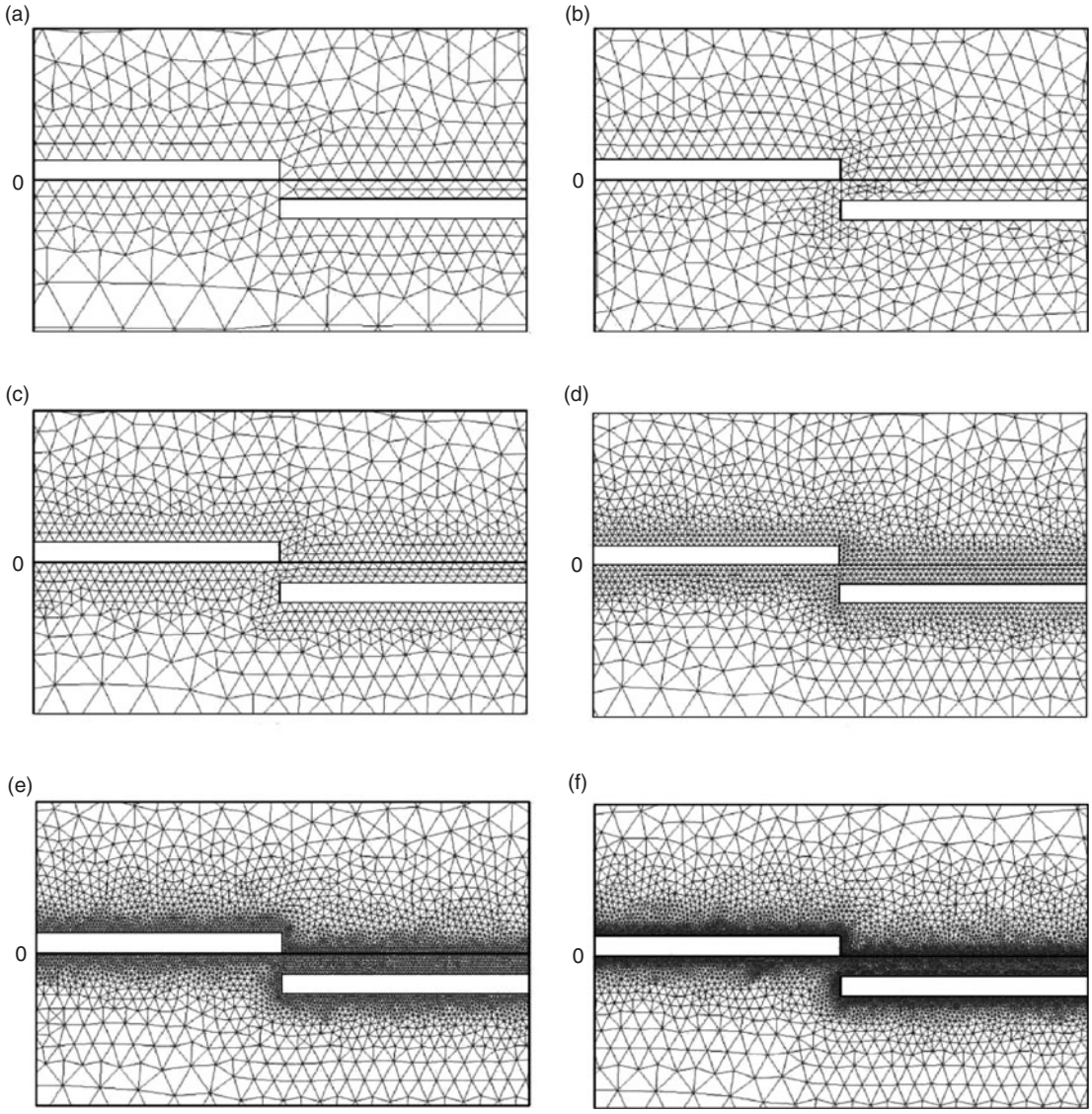

Figure 8. Grid refinement near the electrode boundaries, showing a range of coarse (a) to fine (f) grid settings. The mesh numbers are shown in Table 1.

Table 1. The mesh refinement analysis and DoFs

Case study	Maximum boundary element size (near electrodes) (m)	Degrees of Freedoms (DoFs)	Mesh Number
a	6.7e-3	28511	3666
b	8e-4	170413	25962
c	5e-4	267444	39981
d	3e-4	474924	72694
e	2e-4	737559	114604
f	1e-4	1557194	247503

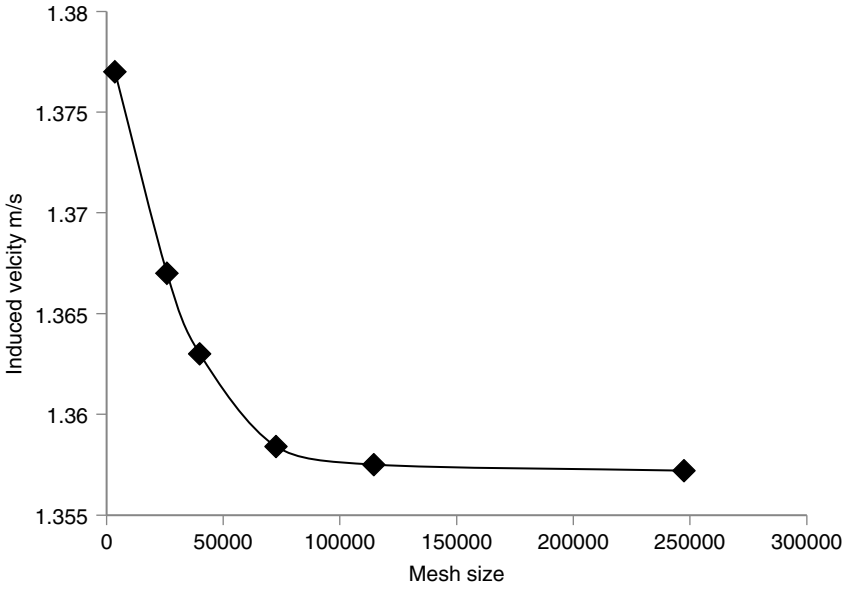

Figure 9. Monotonic convergence of the induced velocity.

Table 2. Results of GCI study for the plasma actuator

	U = maximum induced velocity, with monotonic convergence
N_1, N_2, N_3, N_4, N_5, N_6	**247503, 114604, 72694, 39981, 25962, 3666**
r_{21}	2.1596
r_{32}	1.5765
r_{43}	1.8182
r_{54}	1.5399
r_{65}	1.0818
U_1	1.3770
U_2	1.3670
U_3	1.3630
U_4	1.3584
U_5	1.3575
U_6	1.3572
p	2.720
Φ_{ext}^{43}	2.2211
e_a^{43}	1.3701%
e_{ext}^{43}	2.130%
GCI_{fine}^{43}	2.658%

The results of the verification analysis conducted shows that the choice of grid settings is adequate in producing numerically acceptable results in the grid convergence analysis. Next we proceed with analyzing the results obtained.

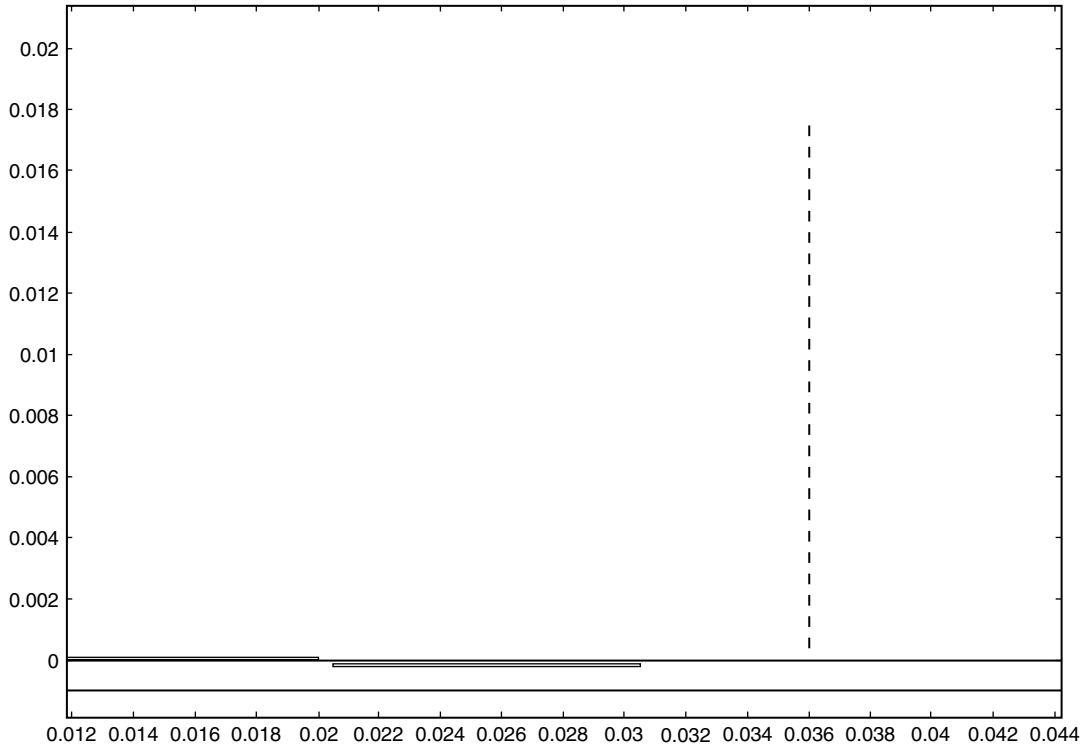

Figure 10. Cut line denoting the last station (1.6 cm downstream of the electrodes interface).

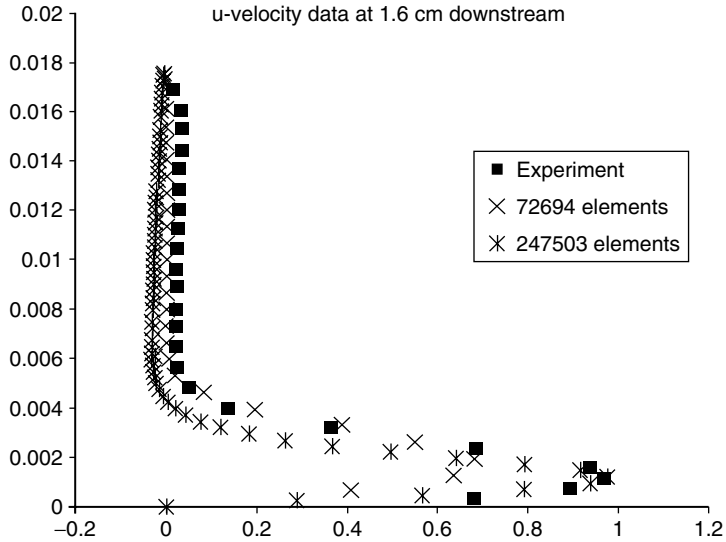

Figure 11. The horizontal velocity profiles for different mesh settings.

7. RESULTS

To ensure that the Fokker-Planck characteristics have been properly implemented, it was necessary to validate that the correct boundary conditions have been inserted. This was done by comparing our results with the graphical characteristics shown in Figure 7. The region above the dielectric surface was of interest because of the expected surface charge growth. Therefore we present a cut line above the dielectric surface, shown as the dashed line in Figure 12, as the one-dimensional representation of

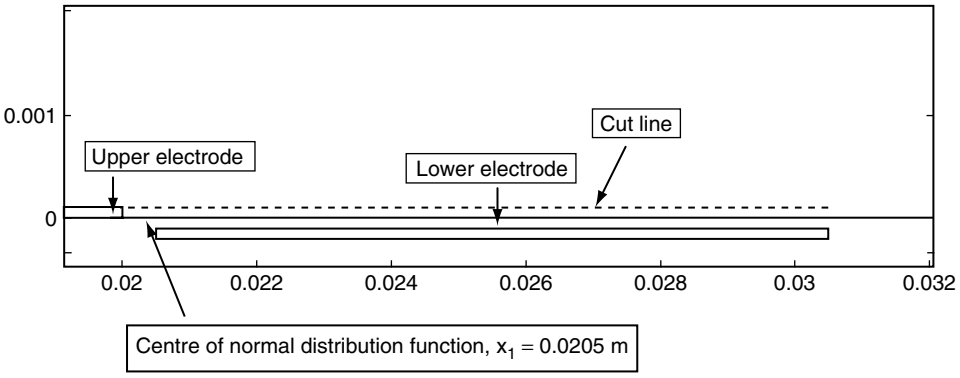

Figure 12. The cut line represented in the geometry.

surface charge density with time and space (x-coordinate). We also note that the position of the centre of the normal distribution function is at x = 0.0205 m. The results obtained are shown in Figure 13.

The results show how the surface charge propagates with nondimensionalised time from $\tau = 0.1$ to 1.0. The choice of the step size would not affect the behavior of the function because the Fokker-Planck characteristics have already been implicitly defined. Hence the magnitude of the step size was chosen to capture the essential physics of the actuator.

The results shown in Figure 13 indicate that at $\tau = 0.1$, the surface charge is still developing near the leading edge of the lower electrode. At $\tau = 0.2$, the surface charge has reached its maximum. The surface charge then dissipates downwards and propagated to the right with increasing time.

The profiles in Figure 13 also prove that the boundary conditions were correctly placed to reproduce the features of the Fokker-Plank propagation and dissipation. The maximums of each successive time-step reduce and their horizontal positions increased, indicating dissipation and propagation. Because of the position of the cutline chosen, the maximums of each time steps reach a plateau. To better visualize

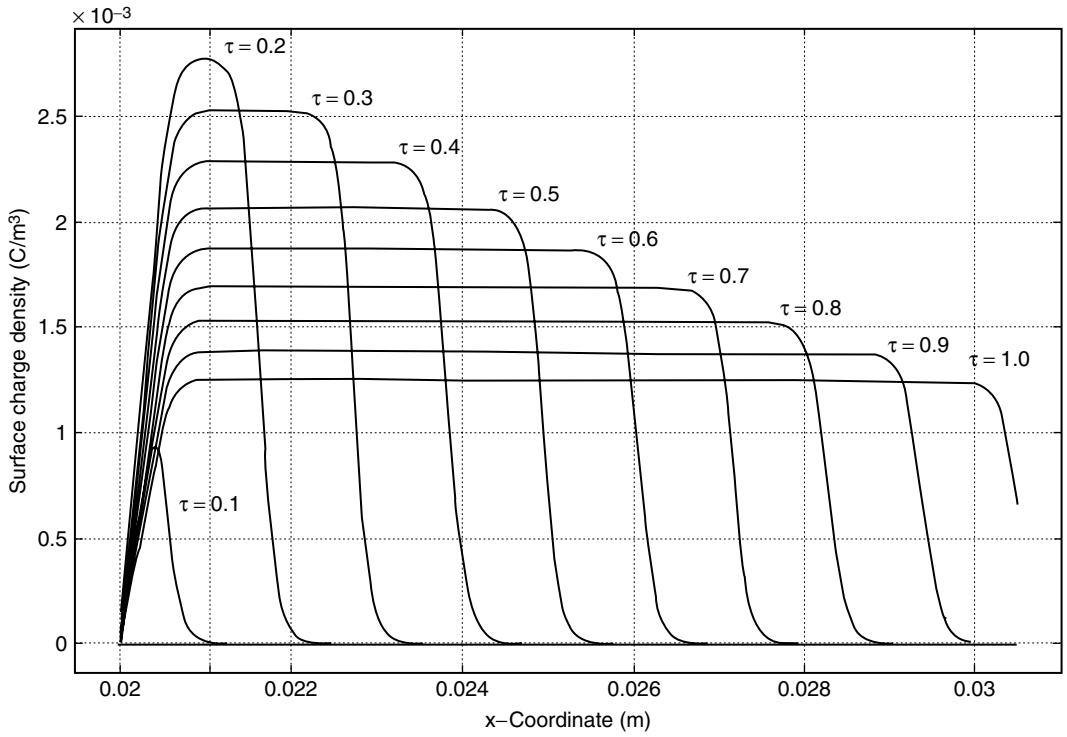

Figure 13. Charge density results obtained from cutline shown in Figure 12. Surface charge density propagation with nondimensionalised time.

the charge density growth, we consolidated figures of charge density growth from $\tau = 0.1$ to 1 (time-step of 0.1) in Table 3 and Table 4.

The figures are in 10^{-4} m dimensions and highlight the propagation features of the boundary conditions. Also, by inspecting the decreasing areas of red plots within each figure, dissipation of the surface charge density can be observed. The surface charge initiates above the left edge of the lower electrode and propagates with time towards the extent of the lower electrode. Subsequently, there is also a dissipation of the surface charge density from the maximum at its initiation. At $\tau = 0.3$, surface charge density covers about 25% of the lower electrode. This increases to 90% at $\tau = 0.9$.

The plots also show detailed surface charge evolution within each non-dimensionalised time step. Each plot range value is from 0 to 4×10^{-3} C/m^3. At $\tau = 0.1$, the surface charge initiates at the gap of the electrodes. It builds up to a maximum of 5×10^{-2} C/m^3 at $\tau = 0.2$ before decreasing steadily from $\tau = 0.2$ to 1.0. At this time ($\tau = 0.1$) the surface charge extends to the length of the lower electrode.

We now proceed to analyze the other variables in the governing equations. The consolidated figures in Table 5 and Table 6 show three variables of interest at the nondimensionalised time, τ from 0.1 to 0.5 and 0.6 to 1.0 respectively. The variables are: electric field (V/m), charge density (C/m^3), Lorentz body force (N/m^3) and induced velocity (m/s). The plot ranges are similar for each variable, only their maximum values vary. The figures show only the area of interest, which is the air domain. The dielectric regions are inactive and hence not coloured. For the first three variables, the focus of the figures is near to the gap of the electrodes to highlight the largest changes/ transients occurring at the region. For the induced velocity plots, the figures show the induced velocities above the encapsulated electrode.

Table 3. Surface charge growth from $\tau = 0.1$ to 0.5

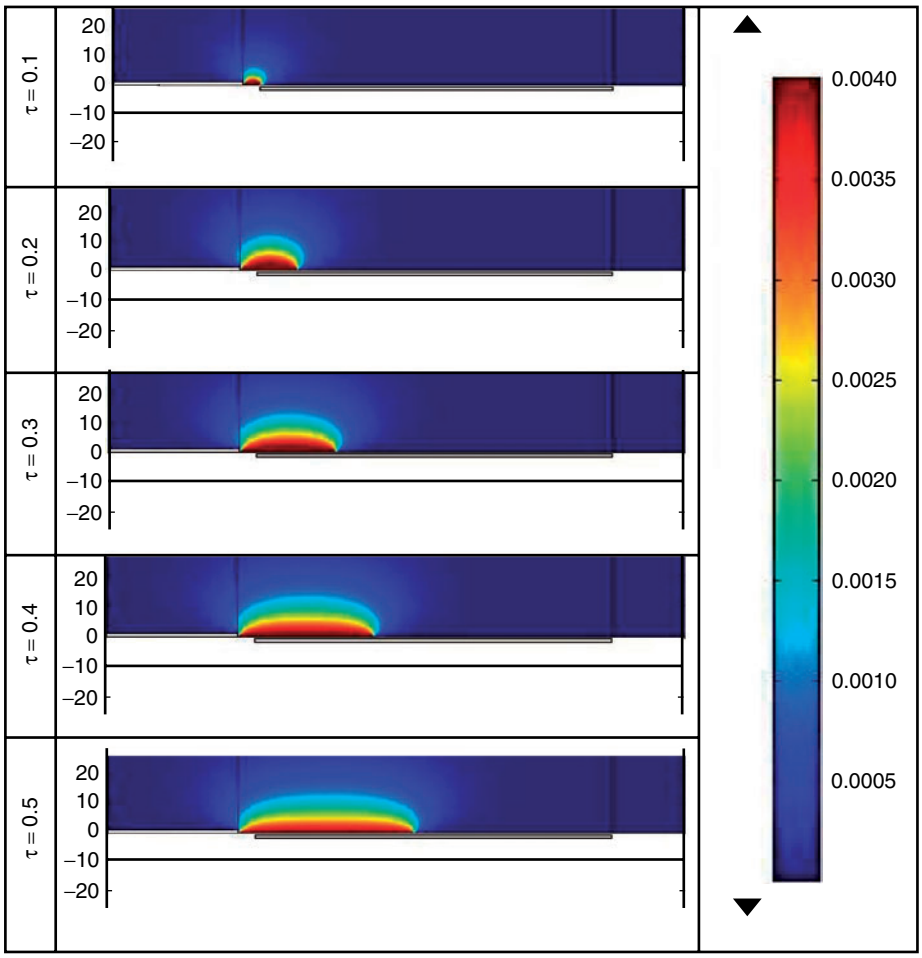

Table 4. Surface charge growth from $\tau = 0.6$ to 1.0

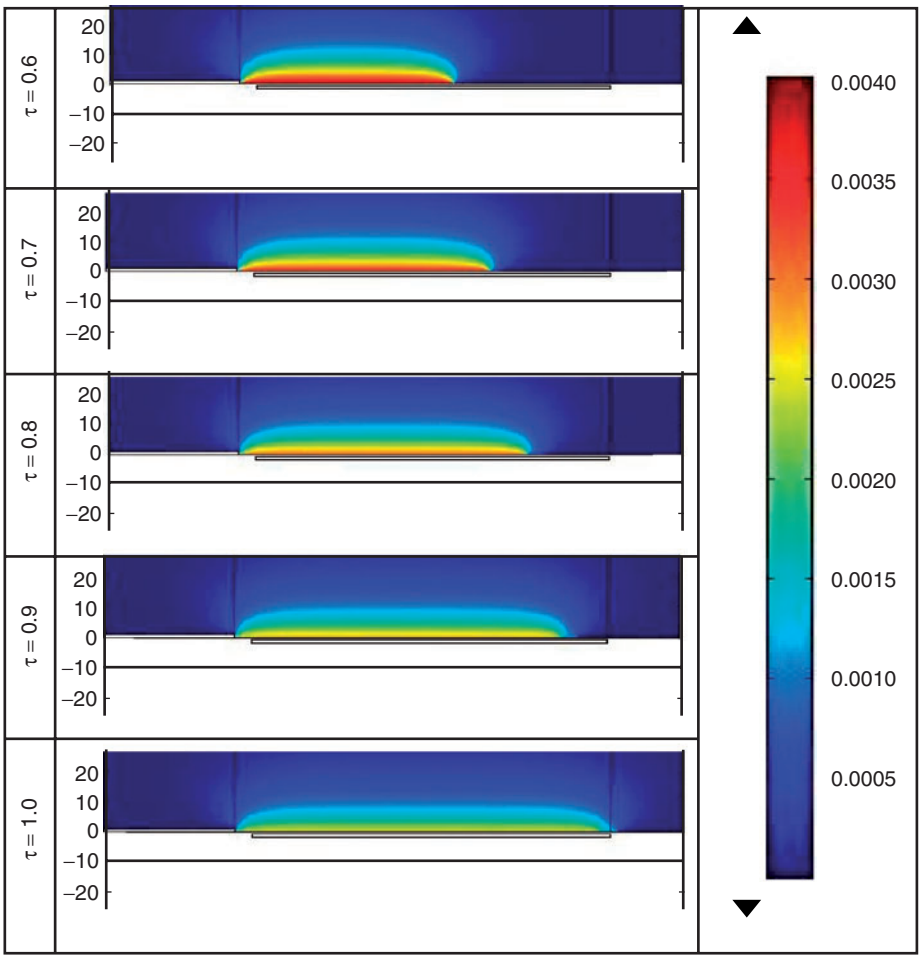

In the first row, the electric field plots range from 0 to 5×10^5 V/m. Primary initiation emerging from the two edges of the upper electrode can be seen for $\tau = 0.1$ and 0.2. Subsequently the electric field increases in both area and magnitude with increasing non-dimensionalised time steps. The magnitude of the electric field reaches it maximum near the gaps of the electrode and decreases in a parabolic profile at the downstream of the dielectric surface. This profile is similar to that observed for the body force propagation.

The second row of figures shows the body force propagation. The plots range from 0 to 1.0×10^4 N/m^3. The body force initiates at the dielectric surface (top left edge of the lower electrode) and reaches a maximum of 1.84×10^4 N/m^3 when $\tau = 0.6$. It then decreases steadily from $\tau = 0.6$ to 1.0.

Finally, in the third row, the induced velocity plots are compared. The plots range from 0 to 1.4 m/s. At $\tau = 0.1$, a small fluid expulsion away from the upper electrode can be seen forming at the gap. The induced velocity above the encapsulated electrode curves towards the upper boundary of the domain at $\tau = 0.2$. The curvature become less prominent at $\tau = 0.3$ and flow develops into a jet from $\tau = 0.3$ to 1.0.

At $\tau = 1.0$, a maximum induced velocity of 1.3 m/s is obtained. The boundary conditions used in the default S-H models produced in a maximum induced velocity of 1.8 m/s. Experimental data by [20, 21] had recorded a maximum reading of 1 m/s. the present result translates to a 50% improvement compared to the default S-H model. The improved boundary conditions showed better velocity agreement due to the dissipations of the charge density and profile of the electric field, resulting in a decreased body force and induced velocity magnitude.

Table 5. Observations of the three variables from τ = 0.1 to 0.5

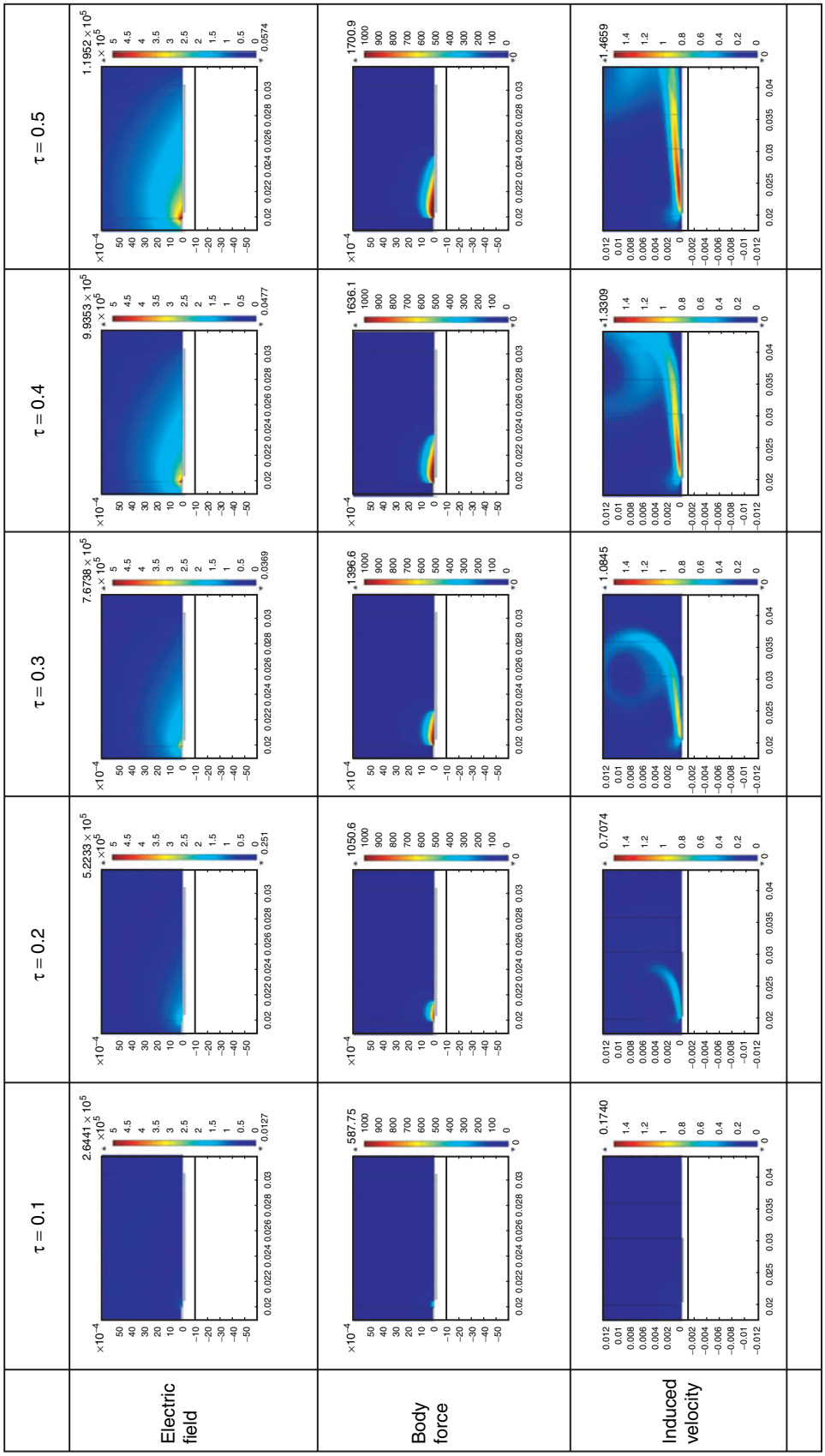

Table 6. Observations of the three variables from $\tau = 0.6$ to 1.0

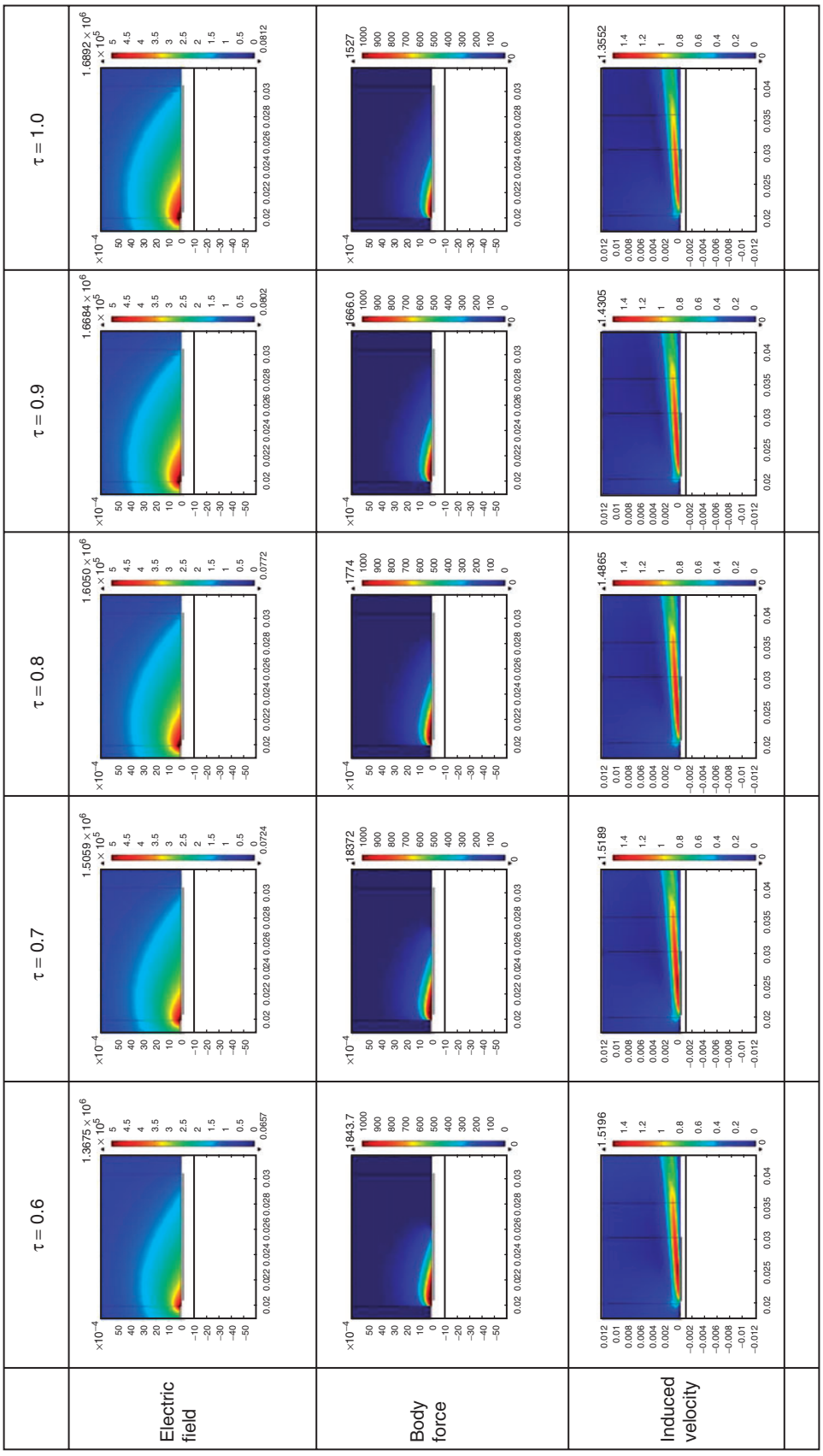

The results can be further improved by imposing the charge density modifications at the lower electrode, instead of the dielectric surface. In the former scenario, simulations resulted in an induced velocity of 1.1 m/s. However, it is unphysical to postulate the charge distributions along the exposed and encapsulated electrodes as boundary conditions.

Two main deductions can be made from the above observations. Firstly, the 'dielectric shielding' boundary condition results in a presence of an electric field above the dielectric surface. In the original S-H model, the electric field was only prominent near the edge of the exposed electrode. The resultant body force shows a larger spread along the dielectric surface. Similarly, the induced velocity profile produces a maximum velocity further downstream. Secondly, the maximum induced velocity occurs at the same non-dimensionalised time step, $\tau = 0.6$. This is because charge density and electric field strength are at their highest at that instant; correlating to the largest body force induced at a value of 1843 N/m^3.

8. CONCLUSION

Modifications to the S-H model have introduced a 'dielectric shielding' condition to the equation governing the electric field, and dissipation and propagation characteristics to the equation governing the charge density. The consolidated figures from the non- dimensionalised time quantity also provided a detailed evolution of the four variables of interest. Our simulation produced an induced velocity of 1.3 m/s which is closer to the experimental value of 1 m/s. Compared to the default boundary condition used in the S-H model which yielded 1.8 m/s, the current result showed about 50% improvement in accuracy. In addition to the two boundary conditions mentioned in the present work, several other boundary conditions above the dielectric surface could be implemented to further enhance the capabilities of the S-H model. The boundary conditions may include spatial and temporal propagation which will be easily configurable to the desired waveform – sine or pulse – as studied in previous charge transport models.

NOMENCLATURE

$\boldsymbol{F_b}$	Lorentz body force (N/m^3)
n_e	electron density (1/m^3),
n_i	ion density (1/m^3)
μ_e	electron mobility (m^2/(sV))
μ_i	ion mobility (m^2/(sV))
$\boldsymbol{E}$	electric field (V/m)
D_e	electron diffusion coefficients
D_i	ion diffusion coefficients
v_i	ionisation frequency (1/s)
r	recombination rate, (m^3/s)
ε_0	vacuum permittivity (F/m)
ε	relative permittivity
e	electron charge (C)
ρ_c	charge density (C/m^3)
Φ	electrical potential (V)
ρ	air density (1.2 kg/m^3)
ϕ	potential influenced by external electric field (V)
φ	potential influenced by net charge density (V)
η	air viscosity (1.8×10^{-5} kg/sm)
U	velocity vector (m/s)
p	pressure (Pa)
t	time (s)
k_1,k_2	breakdown electric field strength constants
$\boldsymbol{F_{tave}}$	time average body force term (N/m^3)
ϑ	frequency of the applied voltage (Hz)

α	factor to account for the collision efficiency
Δt	time during which the plasma is formed (s)
δ	Dirac delta function
λ_D	Debye Length (m)

REFERENCES

[1] Moreau, E., Airflow control by non-thermal plasma actuators. *Journal of Physics D: Applied Physics,* 2007. **40**(3): p. 605–636.

[2] Corke, T.C., Post, M.L., and Orlov, D.M., Single dielectric barrier discharge plasma enhanced aerodynamics: Physics, modeling and applications (Review Article). *Experimental Fluids,* 2009(46): p. 1–26.

[3] Massines, F., Rabehi, A., Decomps, P., Gadri, R.B., SeÌgur, P., and Mayoux, C., Experimental and theoretical study of a glow discharge at atmospheric pressure controlled by dielectric barrier. *Journal of Applied Physics,* 1998. **83**(6): p. 2950–2957.

[4] Boeuf, J.P. and Pitchford, L.C., Electrohydrodynamic force and aerodynamic flow acceleration in surface dielectric barrier discharge. *Journal of Applied Physics,* 2005. **97**(10): p. 1–10.

[5] Rouffet, J.-B. Plasma Actuator Influence on Air Flow. in *COMSOL Conference 2008*. 2008. Hannover: COMSOL.

[6] Roth, J.R., Sherman, D.M., and Wilkinson, S.P. Boundary layer flow control with a one atmosphere uniform glow discharge surface plasma. in *36th Aerospace Sciences Meeting & Exhibit*. 1998. Reno, Nevada.

[7] Orlov, D.M. and Corke, T.C. Numerical simulation of aerodynamic plasma actuator effects. in *43rd AIAA Aerospace Sciences Meeting and Exhibit - Meeting Papers (also in AIAA 2005-1083)*. 2005.

[8] Suzen, Y.B., Huang, P.G., Jacob, J.D., and Ashpis, D.E., Numerical simulations of plasma based flow control applications, in 35th AIAA Fluid Dynamics Conference and Exhibit. 2005. p. 1–11.

[9] Roy, S. and Wang, C.C., Plasma actuated heat transfer. *Applied Physics Letters,* 2008. **92**(23).

[10] Singh, K.P. and Roy, S., Simulation of an asymmetric single dielectric barrier plasma actuator. *Journal of Applied Physics,* 2005. **98**(8): p. 1–7.

[11] Enloe, C.L., McLaughlin, T.E., VanDyken, R.D., Kachner, K.D., Jumper, E.J., and Corke, T.C., Mechanisms and Responses of a Single Dielectric Barrier Plasma Actuator: Geometric Effects. *AIAA Journal*, 2004. **42**(3): p. 595–604.

[12] Shyy, W., Jayaraman, B., and Andersson, A., Modeling of glow discharge-induced fluid dynamics. *Journal of Applied Physics*, 2002. **92**(11): p. 6434–6443.

[13] Enloe, C.L., McLaughlin, T.E., VanDyken, R.D., Kachner, K.D., Jumper, E.J., and Corke, T.C., Mechanisms and Responses of a Single Dielectric Barrier Plasma Actuator: Plasma Morphology. *AIAA Journal*, 2004. **42**(3): p. 589–594.

[14] Orlov, D.M., Modelling and Simulation of Single Dielectric Barrier Discharge Plasma Actuators, in Aerospace and Mechanical Engineering. 2006, University of Notre Dame: Notre Dame, Indiana. p. 189.

[15] Orlov, DM., Corke, T.C., and Patel, M.P., Electric Circuit Model for the Aerodynamic Plasma Actuator. *AIAA Journal*, 2006. **19:** p. 14678–14687.

[16] Suzen, Y.B. and Huang, P.G. Simulations of flow separation control using plasma actuators. in *44th AIAA Aerospace Sciences Meeting and Exhibit AIAA 2006-877*. 2006. Nero, Nevada.

[17] Suzen, Y.B., Huang, P.G., and Ashpis, D.E., Numerical simulations of flow separation control in low-pressure turbines using plasma actuators, in 45th AIAA Aerospace Sciences Meeting. 2007: Toronto, Ontario Canada. p. 11358–11365.

[18] Reasor Jr, D.A., LeBeau Jr, R.P., and Suzen, Y.B. Unstructured grid simulations of plasma actuator models. in *Collection of Technical Papers - 37th AIAA Fluid Dynamics Conference AIAA 2007-39 73*. 2007. Miami, Florida.

[19] Grundmann, S., Klumpp, S., and Tropea, C., Experimental and numerical investigations of boundary-layer influence using plasma-actuators, in Notes on Numerical Fluid Mechanics. 2007. p. 56–68.

[20] Jacob, J.D., Karthik, R., Anthony, R., and Rivir, R.B. Control of Laminar and Turbulent Shear Flows Using Plasma Actuators. in *4th International Symposium on Turbulence and Shear Flow Phenomena*. 2005. Williamsburg, VA.

[21] Santhanakrishnan, A., Reasor Jr, D.A., and LeBeau Jr, R.P., Characterization of linear plasma synthetic jet actuators in an initially quiescent medium. *Physics of Fluids*, 2009. **21**(4).

[22] Roth, J.R., DC Electrical Glow Discharge in Gases, in *Industrial Plasma Engineering Volume 1: Principles*. 1995, Institute of Physics Publishing p. 284–351.

[23] COMSOL, COMSOL Multiphysics Modeling Guide, in *COMSOL 4.2* 2011.

[24] Hindmarsh, A.C., Brown, P.N., Grant, K.E., Lee, S.L., Serban, R., Shumaker, D.E., and Woodward, C.S., SUNDIALS: Suite of nonlinear and differential/algebraic equation solvers. *ACM Transactions on Mathematical Software,* 2005. **31**(3): p. 363–396.

[25] Celik, I.B., Ghia, U., Roache, P.J., Freitas, C.J., Coleman, H., and Raad, P.E., Procedure for Estimation and Reporting of Uncertainty Due to Discretization in CFD Applications. *Journal of Fluids Engineering,* 2008. **130**(7): p. 078001–4.

[26] Ibrahim, I.H. and Skote, M., Modeling the Plasma Actuator via the Splitting of the Electric Potential, in *Icms2010: Proceedings of the Third International Conference on Modelling and Simulation, Vol 2 - Modelling and Simulation in Engineering,* Y. Jiang and X. Chen, Editors. 2010, World Acad Union-World Acad Press: Liverpool. p. 1–6.